The consistent in-situ global gridded temperature and salinity dataset, CORA OA 1960-2024

Tanguy Szekely[1] and Jean-Renaud Miadana[1]

[1]Société coopérative ARL OceanScope, 38 rue Jim Sevellec, 29200, Brest

Correspondence: Tanguy Szekely (tanguy.szekely@ocean-scope.com)

Abstract.

Gridded ocean products play a pivotal role in oceanographic and climate research, providing a framework for the cross-validation and calibration of satellite observations and in-situ data. This paper describes the latest evolution of the global gridded ocean objective analysis fields for temperature and salinity, distributed by the Copernicus Marine Service. It accounts for the update of the objective analysis first guess using monthly fields derived from the temporal interpolation of World Ocean Atlas 2023 (WOA23) decadal temperature and salinity climatologies. The new product provides monthly objective analysis fields for temperature and salinity with a 0.5° horizontal resolution and 187 vertical levels covering depths from 0 to 5500 m. The dataset is updated annually and covers the period from 1960 to December of the last complete year; the version described here covers 1960–2024. A full reprocessing is conducted every November, while an interim update covering the first six months of the current year is released each June. This product was compared with other reference 3D temperature and salinity datasets, as well as SST and SSS products. It exhibits strong consistency with all reference data, particularly over the 1985–2024 period. Notably, the product proved robust against the "Argo fast salty drift" frequently detected in other datasets after 2016. The gridded product is freely accessible on the Copernicus Marine data store (https://data.marine.copernicus.eu/) under the ID INSITU_GLO_PHY_TS_OA_MY_013_052.

1 Introduction

According to IPCC (2023), the global ocean has warmed and the salinity changes observed since the mid-20th century are predominantly driven by anthropogenic forcing. To investigate these processes, the scientific community has developed an extensive suite of instruments for measuring ocean temperature and salinity. International initiatives were subsequently established to coordinate basin-scale measurement campaigns Chapman (1998); Bourlès et al. (2008); Teng et al. (2008) and to implement sustained observation systems such as the Global Drifter Program Niiler (2001). This international cooperation culminated in the late 1990s with the development of the Argo program Roemmich et al. (2009); Jayne et al. (2017), which achieved near-global coverage to 2000 m by 2008 and extended observations to depths exceeding 5500 m by 2016.

The Coriolis Ocean dataset for ReAnalysis (CORA) was initiated by the French Coriolis project in 2008, incorporated into the European MyOcean project in 2010 Bahurel et al. (2010); Cabanes et al. (2013), and subsequently integrated into the Copernicus Marine Service Le Traon et al. (2019). It is provided as a delayed-mode, quality-controlled global in situ temperature and

salinity dataset, with the objective of delivering a high-quality record that includes carefully assigned quality flags and adjusted parameter values when available. CORA has been widely employed, particularly for ocean reanalysis applications Lellouche et al. (2021), as well as for global ocean heat content assessments von Schuckmann and Le Traon (2011); von Schuckmann et al. (2013, 2023).

Since 2010, the CORA in situ dataset has been complemented by an objective analysis designed to provide a smooth three-dimensional representation of the monthly ocean temperature and salinity fields derived from it. This analysis has been yearly to twice yearly updated and extended using successive versions of the ISAS tool Gaillard et al. (2009); Gaillard (2012); Gaillard et al. (2016), and in its most recent release covers the period from the 1960s to the present.

The present article introduces the latest version of the CORA objective analysis product, which is distributed through the Copernicus Marine Service (https://doi.org/10.17882/46219). Section 2 describes the data sources used to produce the objective analysis. The processing steps, methodology, and parameter settings are presented in Section 3. The resulting product is evaluated against comparable datasets in Section 4. Finally, conclusions and perspectives for future developments are provided in Section 5.

2 Data

2.1 Data source

This product is based on the temperature and salinity profiles extracted from the INSITU_GLO_PHY_TS_DISCRETE_MY_013_001 product, distributed by the Copernicus Marine Service (CMEMS, 2025). This product is itself derived from the near–real-time (MYNRT) global in situ product INSITU_GLO_PHYBGCWAV_DISCRETE_MYNRT_013_030, with additional delayed-mode validation performed using the methods described in Szekely et al. (2019), Gourrion et al. (2020), and Szekely (2024b). It provides a complete collection of profiles from 1950 to 2024. Additionally, it benefits from the synchronization of the Copernicus Marine MYNRT dataset with major data providers (World Ocean Database, Argo, etc.), ensuring that the best available version of each profile remains with adjustments made by the original providers.

Figures 1, 2, and 3 provide insights into the data availability for the various data types used to produce the objective analysis. The “Bottles” category consists of measurements obtained by directly sampling seawater using bottles deployed along a cable. Since there are only a limited number of bottles on each cable, most bottle profiles contain relatively few measurements, often taken at standard depths (see Fig. 2, top right panel). On the other hand, bottle profiles have made it possible to reach depths below 5500 m as early as the 1950s. The decrease in the yearly number of bottle data collected during the 2000s is mainly due to the difficulty of measurement. Most recent sampling is carried out with Rosette systems, which often group 10 to 20 bottles and can collect seawater at many vertical levels. However, the Rosette is heavy and must be deployed on a steel cable with a winch. Collecting samples from deep water therefore requires an oceanographic vessel equipped with a crane, and a single profile can take several hours to complete.

The XBT and MBT instruments are bathythermographs deployed either along a cable (MBT) or as free-falling expendable probes (XBT) to measure ocean temperature. XBT casts can reach only a limited set of maximum depths, which appear as

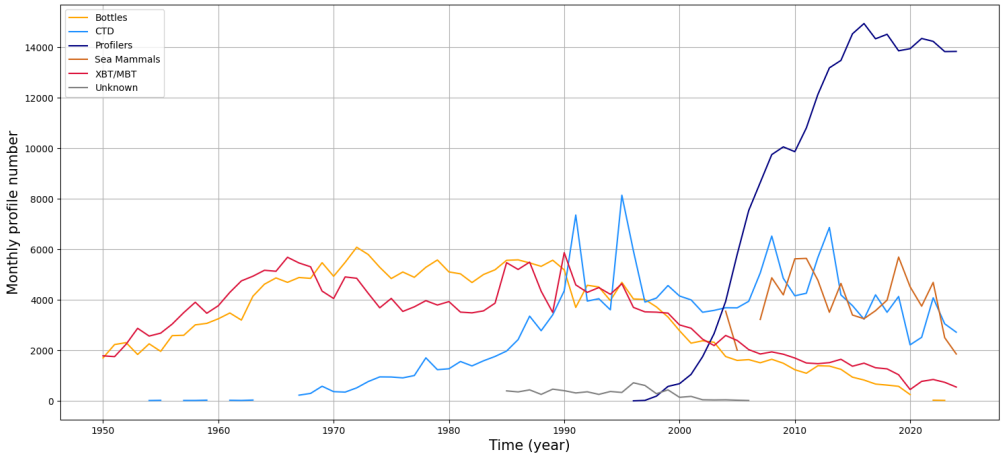


Figure 1. Number of profiles distributed in `INSITU_GLO_PHY_TS_DISCRETE_MY_013_001` as a function of instrument type. Only profiles from the 1960–2024 period are used for the objective analysis.

steps in the number of available data points in Fig. 2 (middle right). The depth of XBT measurements is estimated from the instrument's fall rate, a process that is susceptible to measurement errors. In the CORA dataset, XBT profiles are adjusted using the correction scheme of Cheng et al. (2014). This scheme determines fall-rate and offset correction coefficients by comparing co-located CTD and XBT profiles. The calculated coefficients vary with both the year and the probe type. However, CORA data processing has shown that, even after correction, some XBT casts can still introduce systematic temperature anomalies in the objective analysis, which have been excluded from the analysis. These excluded profiles are not shown in Figure 2 (middle). Contrary to CTD casts, XBTs can be deployed from moving ships. As a result, Figure 2 (middle left) shows a higher density of profiles along the main shipping routes.

CTDs (Figure 2, bot.) are conductivity-temperature-depth casts, where salinity is derived from conductivity and temperature measurements. They are mostly deployed along cables from oceanographic ships, providing high vertical resolution profiles (often with more than one data point per dbar). The towed undulating CTD profiles available in the dataset from the 2000s are also classified as CTDs in this index. Like bottle casts, most CTDs are deployed from oceanographic ships at station and require several hours to complete. As a result, the number of CTD casts is lower in the Southern Ocean, leaving large areas uncovered.

The animal-mounted profiles (Fig. 3, top) come from CTD-like sensors deployed mostly on marine mammals and sea turtles. These instruments measure temperature and salinity along the animals' dives and often transmit low-resolution profiles when the animal surfaces to breathe. After a few months, if the instruments are retrieved, they provide access to the full high-resolution data. Major deployment sites include the Kerguelen Islands, the west coast of North America, the Labrador Sea, and Greenland, i.e. high latitude areas. These deployments have yielded valuable observations along the seasonal migration routes

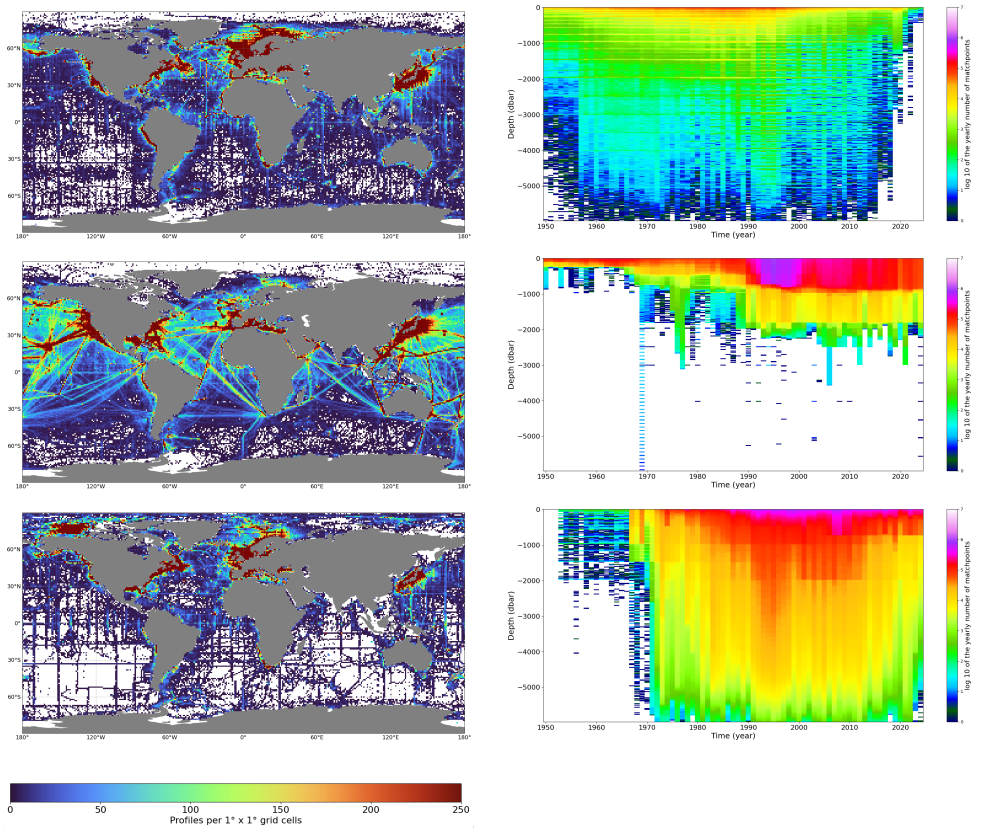


Figure 2. Left: Number of in-situ casts in 1-degree square grid cells from 1950 to 2024. **Right**: Yearly number of measurements in 20-meter vertical depth bins from 1950 to 2024. **Top** : Bottles casts. **Mid.** : XBT/MBT casts. **Bot.** : CTD casts.

of marine mammals, particularly in the Southern Ocean. Most profiles extend through the upper 1000 m of the ocean, with fewer reaching depths of up to 2000 m. The MYNRT dataset gathers both adjusted profiles extracted from the MEOP (Marine Mammals Exploring the Oceans Pole to Pole) database and profiles originating from other sources (near-real-time versions of profiles, independent programs, etc.). All of these profiles are validated through the same procedures described above to ensure the homogeneity of the final dataset, even though the prevalence of errors is markedly lower among MEOP-sourced profiles than among other near-real-time profiles.

Argo profiles have been the most important deep-ocean observing system since the 2000s, providing near-global coverage with high data availability. The project was conceived in 1998 with the goal of deploying a network of autonomous profiling floats drifting freely at depth. These profilers have been deployed continuously since then, with a target of more than 3000 permanently operational floats covering the global ocean between 60°N and 60°S. The large-scale deployment of Deep Argo floats in 2015–2016 has further strengthened the vertical coverage, as these instruments can reach depths of 6000 m compared to 2000 m for the historical floats, as shown by the deepening of the data coverage in Figure 3 (middle right).

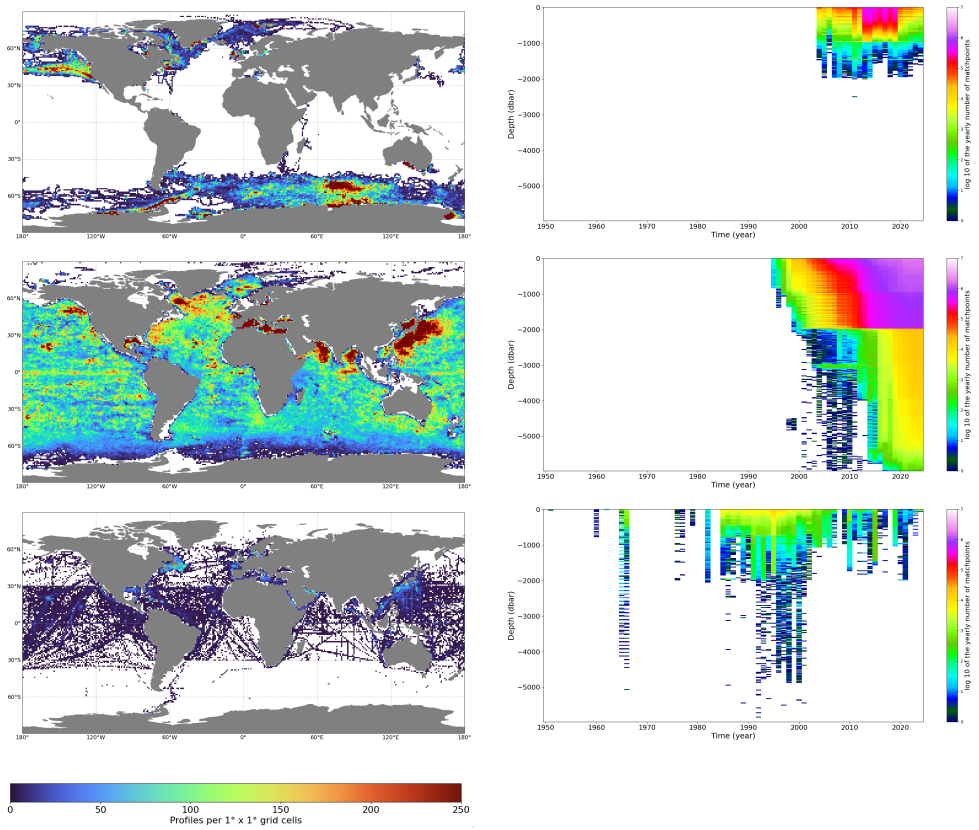


Figure 3. Left: Number of in-situ casts in 1-degree square grid cells from 1950 to 2024. **Right**: Yearly number of measurements in 20-meter vertical depth bins from 1950 to 2024. **Top**: Animal-mounted casts. **Middle**: Autonomous profiler casts. **Bot.**: Unknown type casts.

The last data type shown in Fig. 3 corresponds to casts of unknown origin. The step increase in the number of available measurements at 1000 m between 1990 and 2010 (Fig. 3, bottom right), together with the profile distribution along the main shipping routes (Fig. 3, bottom left), suggests that many of these casts are in fact XBT profiles. Historical data were first only integrated in mid latitude, which explain the sharp decrease in the number of unknown casts north of 30°N and south of 35°S.

3 method

3.1 Data selection and vertical interpolation

Data selection and vertical interpolation are key steps for ensuring the accuracy of the objective analysis. For each month covered by this objective analysis product, the relevant temperature and salinity profiles are extracted from the CORA dataset and assembled into monthly data files. Because the analysis time is centered on the 15th of each month with a 20-day temporal correlation length, successive monthly files necessarily overlap. Only data points with quality-control flags of *good* or *probably*

good (QC = 1 or 2) are retained. The remaining gaps are then filled by linear interpolation onto the product's vertical grid. Finally, new QC flags are applied to the interpolated profiles, excluding interpolated points where the distance from the nearest original observation exceeds 16 times the vertical bin width.

The objective analysis (OA) then further filters the validated data to remove observations that deviate from the reference field. The method developed by Bretherton et al. (1976) requires prior knowledge of the statistical characteristics of the interpolated field. In the case of CORA OA dataset, this filtering step is designed to remain consistent with sub-mesoscale variability, imposed by the parameterization of equation 6, particularly in the deep ocean. Observations that differ from estimated thresholds from the reference are filtered out to avoid propagating small-scale dynamics into the sub-mesoscale analysis.

To filter the observations, temperature and salinity profiles are compared to the climatological field described in Section 3.2. Equations 1 and 2, for temperature and salinity respectively, are designed to detect data points that deviate from the climatology, with relaxed constraints in regions of high vertical variability. Data points that do not meet these conditions are flagged as bad before the vertical interpolation step. The T_{clim} and S_{clim} values are extracted from the ISAS 17 standard deviation climatology Kolodziejczyk et al. (2019). In this version of CORA OA, we have set $\alpha = 6$ and $\beta = 2$, consistently with Kolodziejczyk et al. (2019) dataset parameterization .T_{STD} and S_{STD} are gridded fields of temperature and salinity standard deviation **??**.

$$\|T - T_{clim}\| < \alpha T_{STD} + \beta \left\| \frac{dT_{clim}}{dz} \right\| \tag{1}$$

$$\|S - S_{clim}\| < \alpha S_{STD} + \beta \left\| \frac{dS_{clim}}{dz} \right\| \tag{2}$$

Finally, the observed profiles must be interpolated onto the 186 vertical levels of the objective analysis. The scheme is a standard linear interpolation using only data points flagged as good or probably good (i.e., parameter and pressure/depth quality control flags lower than 3). To account for the reduced observational accuracy due to vertical interpolation, the method proposed by Gaillard et al. (2016) increases the assigned measurement error to a threshold when the vertical distance between two consecutive observations exceeds the vertical resolution of the analysis grid (see Eq. 3). Consistently with Kolodziejczyk et al. (2019) and Gaillard et al. (2016) parameterization, the measurement error is multiplied by a dimensionless factor of 4 when $2 <$ threshold < 4, by a dimensionless factor of 9 when $4 <$ threshold < 8, and by a dimensionless factor of 16 when $8 <$ threshold < 16. When threshold > 16, the data point is excluded from the analysis.

$$Thres = \frac{dz_{obs}}{dz_{grid}} \tag{3}$$

3.2 Climatology

In the objective analysis framework presented by Bretherton et al. (1976) and further developed into the In Situ Analysis System (ISAS) tool by Gaillard et al. (2016), the analysis is performed on temperature and salinity anomalies relative to reference

fields. The choice of these reference fields is therefore crucial for minimizing the objective analysis error. Moreover, during the 1960–2005 period, in-situ profiles did not cover most of the global ocean. Consequently, the analysis converges toward a solution close to the measurements in regions with good observational coverage, but tends toward the climatology in poorly sampled areas. Climatologies covering decadal periods have been used as first guesses in previous versions of the objective analysis (Szekely, 2024a) despite the fact that this approach introduces discontinuities between the end of one climatology and the beginning of the next one. This was particularly evident in the integrated metrics such as global ocean heat content that were biased by the first-guess climatology and failed to represent the detectable effects of long-term warming.

The first guess adopted is calculated from the WOA decadal climatology (Reagan et al., 2024). Each month reference field is a linear interpolation using two decadal climatologies except for the more recent years. For example, the January 1973 first-guess field is derived from a linear interpolation between the January fields of the 1965–1974 and 1975–1984 climatologies.

3.3 Objective analysis

3.3.1 Method

Following the methodology described in Gaillard et al. (2016), the objective analysis is performed by mapping the data anomaly $(y - y_{ref})$ onto a regular grid using a gain matrix (see Eq. 4).

$$x = x_{ref} + K^{OI}(y - y_{ref}) \tag{4}$$

With,

$$K^{OI} = C_{ao}(C_{oo} + R)^{-1} \tag{5}$$

"With $R_{ii} = \sigma^2_{URi} + \sigma^2_{MRi}$, the matrix R represents the sum of the error due to unresolved scales and the measurement error for observation i. The covariance matrices C_{ao} and C_{oo} represent, respectively, the covariance between the analyzed field and the observations, and the covariance of the reference field in the observation space. Both are defined using the following function:

$$C(dx, dy, dt) = \sum_{i=1}^{2} \sigma^2_{Li} exp\left(\frac{dx^2}{2L^2_{xi}} + \frac{dy^2}{2L^2_{yi}} + \frac{dt^2}{2L^2_{ti}}\right) \tag{6}$$

Where dx, dy, and dt are the spatial and temporal distances, and L_x, L_y, and L_t are the corresponding correlation scales. The spatial scales of the first Gaussian component (L_{x1} and L_{y1}) are constant and set to 300 km . The spatial scales of the second Gaussian component are proportional to the Rossby radius associated with the first baroclinic mode. Both temporal scales, L_{t1} and L_{t2}, are set to 30 days. The parameters choice are consistent with Gaillard et al. (2016).

3.3.2 Data distribution and statistics

Fig.4 (Top) shows the amount of data available in each file and at each vertical level. The step-like patterns in data density observed above 1000 m and 2000 m depth before 1990 reflect the nature of data distribution during that period. Most deep profiles available at that time were bottle casts, characterized by very low vertical resolution (see Fig.2, Top Right). The vertical interpolation algorithm described in Section 3.1 tends to eliminate interpolated values that are too far from the original observation points. This pattern tends to disappear as bottle casts where completed by other observation casts after 1990. hlThe vertical interpolation criterion described in Eq.3 is therefore a likely contributor to this artefact, and will be revised in future versions of the dataset in order to reduce this problem. After the 2000s, data density is dominated by ARGO profiles, with a sharp decrease near 2000 m depth corresponding to the maximum profiling depth of most early ARGO floats. This limitation was reduced after 2016 with the wider deployment of deep ARGO floats.

Fig. 4, Bot. shows the median temperature and salinity anomaly between the objective analysis profiles and the climatologies. Above 1000m depth, the median anomaly reaches amplitudes over 0.1 °C, decreasing over time, with alternating patches of positive and negative values. This behavior is expected, as the linear interpolation of climatologies cannot capture the interannual variability of ocean temperature. Below 1000m depth, the median anomaly is predominantly negative, with a decreasing amplitude over time. Table 1 shows that the mean temperature anomaly decreases from 0.006 °C in the 0–500m depth layer to 0.004°C in the 2001–5500m layer. Occasional larger anomalies at depth are associated with months where very few profiles are available, and are therefore statistically insignificant. The median salinity anomaly (see table 2) is higher above 500m depth, with significant temporal variations, although it remains two orders of magnitude lower than the temperature anomaly. As expected, the noise decreases over time below 1000m depth.

	5^{th} percentile	Mean	95^{th} percentile
0-500 m depth	-0.08	0.006	0.1
501-1000 m depth	-0.02	0.003	0.4
1001-2000 m depth	-0.009	0.004	0.03
2001-5500 m depth	-0.004	0.004	0.02

Table 1. Mean temperature anomaly between profiles and climatology and 5 and 95 percentiles. Unit : Degrees Celsius

	5^{th} percentile	Mean	95^{th} percentile
0-500 m depth	-0.03	0.002	0.01
501-1000 m depth	-0.004	0.0001	0.004
1001-2000 m depth	-0.003	-0.0002	0.002
2001-5500 m depth	-0.001	-6*10^{-6}	0.002

Table 2. Mean salinity anomaly between profiles and climatology and 5 and 95 percentiles. Unit : PSU

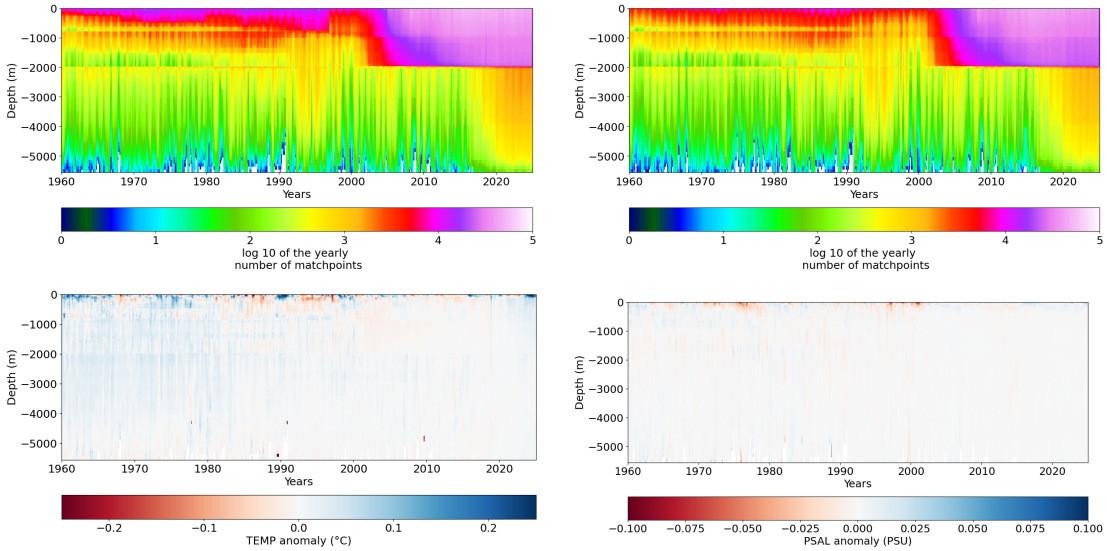


Figure 4. Top: $\log_{10}$ of the number of data points per month and per vertical level in the objective analysis files. Bottom: After Mapping monthly median profile anomalies. Left: Temperature; Right: Salinity.

3.4 Comparison datasets

Three in-situ 3D gridded products and two surface gridded products are used to evaluate the objective analysis results. Hereafter, IAPv4 will refer to the IAPv4 ocean temperature and salinity dataset from the Institute of Atmospheric Physics (Cheng et al., 2024a). EN4 will refer to the Met Office Hadley EN4 ocean temperature and salinity objective analysis dataset Good et al. (2013); Killick (2021). ISAS 20 will refer to the ISAS 20 ARGO objective analysis (Kolodziejczyk et al., 2023), which is an analysis performed at the LOPS/UMR using the same tool as the CORA products, but with ARGO floats only. ERSST will refer to the extended reconstructed sea surface temperature dataset (version 6) by NOAA (Huang et al., 2025). SSS L4 will refer to the satellite-based SSS product Sammartino et al. (2022). This product was preferred over other SSS products since its combined in-situ/satellite and SST/SSS approach allows it to extend its time coverage back to 1993, in contrast to products based solely on satellite-measured SSS (e.g., from L-band radiometry missions such as SMOS, Aquarius, or SMAP), which only cover the 2010-2025 period.

4 Results

4.1 SST trend

The upper layer of the CORA OA mean temperature anomaly time series is compared with three international reference 3D datasets (IAPv4, EN4, and ISAS 20) and one SST dataset (ERSST) (Figure 5). All time series in Figure 5 are expressed as anomalies relative to their mean over the period common to all products (2002-2020), so that differences in absolute level

and in temporal coverage do not affect the comparison. Trends are computed over the available period of each product, and are therefore directly comparable only between products of identical coverage. The sea surface warming trend value and the associated 90% confidence interval shown by all products are calculated using a LOWESS method Cheng et al. (2022a). In all basins, the CORA mean SST warming rate falls within the range of the warming rates of the other products. The agreement between products is very good in the global ocean and in the Atlantic basin. However, there are discrepancies: EN4 shows a lower temperature anomaly in the Pacific, Indian, and Southern Oceans during 2005–2022, and ERSST shows lower anomalies during 1960–1970 in the same basins. In addition, CORA appears to exhibit lower interannual variability, particularly in the Southern Ocean and Indian Ocean, despite the good overall agreement in the tendency. These regions also show limited data availability across all data types compared with the Atlantic Ocean and the North Pacific (see Figures 2 and 3). We can therefore assume that the reduced interannual variability is partly a consequence of the scarcity of available profiles. However, the CORA OA product also exhibits low interannual variability after 2005, when the Argo program reached near-global coverage. It is then possible that this smoothed interannual variability results from the specific parameterization of the correlation function used in the objective analysis (see Equation 6).

In all cases, the IAPv4 warming trend lies in the lower percentile compared to other products, while CORA tends to be in the upper percentile. This is likely due to EN4, CORA, and ERSST that include the years 2023 and 2024, which exhibit record-high global sea surface temperature anomalies (Huang et al., 2024; Terhaar et al., 2025). When restricting the calculation of warming trends to years prior to 2023, the spread among products is reduced: CORA: 0.93 ± 0.06°C/century, ERSST: 0.93 ± 0.23°C/century, EN4: 0.87 ± 0.23°C/century, IAPv4: 0.79 ± 0.27°C/century, ISAS20: 1.0 ± 0.7°C/century. In this case, only ISAS20 departs from the other analyses, but it covers only 2002–2020, a period during which the ocean warming rate is higher than before the 2000s (Cheng et al., 2022b). In nearly all comparisons, the ERSST warming rate diverges from other products, since ERSST mean temperatures are systematically lower than any other datasets in all basins during the 1960s. Conversely, the CORA warming rate shows smaller 90% confidence interval than other products, likely due to the lower interannual variability of the CORA OA time series, particularly before the ARGO era. The ocean basin with the largest spread in mean SST time series is the Southern Ocean (lat < –35°N). In this basin, all products except ERSST show overall good agreement until 2000. After that, the spread increases: EN4 and ISAS20 provide the lowest estimates, IAPv4 and ERSST the highest, while CORA remains close to the median. In this basin, the lack of data prior to the 2000s is striking (see Fig. 2). This situation improved in the 2000s with the development of ARGO floats and the use of animal-mounted CTDs (see Fig. 3). Although animal-mounted CTDs provide valuable profiles, they are prone to data drift and sensor malfunctions due to challenging deployment conditions. The CORA validation process efficiently detects and flags failed instruments, thereby reducing the influence of sensor drift (Szekely et al., 2019; Szekely, 2024b), however, we cannot compare our profile selection with that used by other products. Consequently, it is difficult to determine whether the spread among products is driven by differences in data availability, data validation, or first guesses.

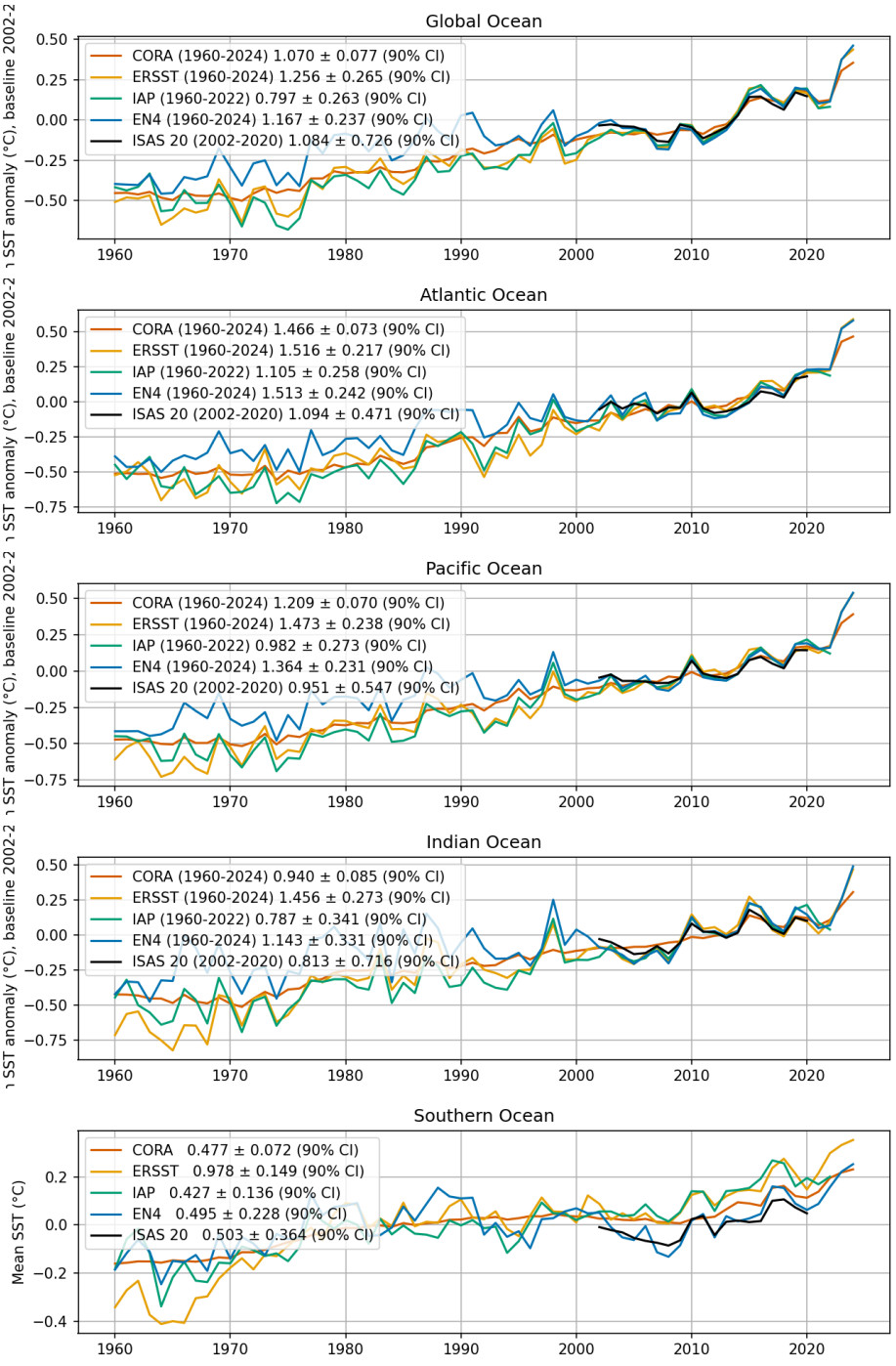


Figure 5. Mean SST and trends for CORA, EN4, IAPv4, ERSST, and ISAS 20 for the global ocean, Atlantic Ocean, Pacific Ocean, Indian Ocean, and Southern ocean (Latitude <-35°N).

		1960–1984	1985–2005	2006–2020
CORA	Global	0.018	0.018	0.026
	Pacific	0.020	0.024	0.023
	Atlantic	0.022	0.033	0.025
	Indian	0.022	0.018	0.031
	South	0.005	0.004	0.020
EN4	Global	0.067	0.065	0.058
	Pacific	0.076	0.073	0.060
	Atlantic	0.065	0.077	0.060
	Indian	0.110	0.100	0.077
	South	0.050	0.039	0.051
ERSST	Global	0.069	0.061	0.057
	Pacific	0.076	0.077	0.057
	Atlantic	0.077	0.081	0.051
	Indian	0.095	0.095	0.084
	South	0.041	0.041	0.039
IAP v4	Global	0.072	0.059	0.059
	Pacific	0.072	0.079	0.063
	Atlantic	0.069	0.084	0.061
	Indian	0.100	0.095	0.078
	South	0.062	0.038	0.040
ISAS 20	Global	–	–	0.045
	Pacific	–	–	0.044
	Atlantic	–	–	0.042
	Indian	–	–	0.057
	South	–	–	0.032
SMOS	Global	–	–	–
	Pacific	–	–	–
	Atlantic	–	–	–
	Indian	–	–	–
	South	–	–	–

Table 3. Detrended standard deviation of the SST by ocean basin and by sub-period

	1960–1984	1985–2005	2006–2020
ERSST	0.069	0.060	0.046
IAP	0.081	0.060	0.045
EN4	0.074	0.082	0.046
ISAS 20	–	–	0.026
SMOS	–	–	–

Table 4. SST RMS differences

4.2 SSS trend

The upper layer of the CORA OA salinity analysis is compared to the EN4, ISAS 20, and IAPv4 upper layers, as well as to the SSS L4 product (Figure 6). This comparison is limited to regions where the bathymetry exceeds 1500 m, in order to reduce

the influence of low-salinity coastal areas, which are more pronounced in the higher-resolution products (SSS L4 and IAPv4) than in the others. At the global scale and across all ocean basins, the CORA product generally aligns more closely with EN4 than with IAPv4 during the pre-ARGO era. An exception occurs in the late 1990s, when the EN4 signal rises to the level of the IAPv4 product for the Global Ocean (0.02 PSU difference), Atlantic Ocean (0.05 PSU), and Pacific Ocean (0.03 PSU). During this period, the CORA signal is closer to the SSS L4, with no sign of SSS sharp variation. The spread among products decreases during the ARGO era (2005–present), with all datasets showing good agreement, especially after 2010, thanks to greater data availability. An exception is the consistently higher salinity values in the EN4 product in the Southern Ocean. In this basin, CORA converges toward IAPv4 after 1985 and shows very good agreement with all products except EN4 in the 2000s which exhibits higher mean salinity with the discrepancy widening after 2015. A closer inspection of the monthly surface salinity fields reveals that this large negative anomaly originates from a well-defined, large-scale feature located in the eastern Indian Ocean and the western Pacific Ocean, with amplitudes exceeding -1 PSU relative to the 2004-2010 climatology. This anomaly pattern and amplitude are unique to the IAPv4 product during this specific period and are not found in the other SSS products used in this study, suggesting that it reflects a product-specific artifact in IAPv4 rather than a genuine oceanographic signal. For SSS, as for SST, CORA displays lower interannual variability than the other reference products, although the long-term variability remains very similar. This finding is consistent with what was reported for SST in Section 4.1. In the case of SSS, the reduced interannual variability of CORA is likely influenced by the 30-day time scale used in the correlation function (see equation6). This time scale is longer than the characteristic variability of large river plume systems, even in open-ocean regions (Fournier et al., 2017; Varona et al., 2019; Boutin et al., 2021; Shi and Wang, 2024).

Table 3 and 5 give the detrended standard deviation of the SST and SSS time series for all tested products and for three periods. It shows that CORA almost always gives a lower estimate of the detrended SSS or SST variability, by a factor of 2 to 10. The most severe underestimation occurs before the Argo era in the Southern Ocean, and the gap narrows markedly during the Argo era. It is consistent with a damping of the objective-analysis signal in regions and periods where data coverage is sparse. The comparison also shows that ISAS20 underestimates the detrended standard deviation relative to the other products, though to a lesser extent than CORA. This is likely related to the linear vertical interpolation scheme shared by CORA and ISAS20 (see Section 3.1), which does not extrapolate to the surface for profiles whose shallowest observation lies below 1 m depth, reducing the number of valid surface data points relative to the other products. The residual gap between CORA and ISAS20 likely reflects a difference in data sources: ISAS20 uses the full Argo profiles from the Global Data Assembly Center, whereas CORA discards Argo sub-surface measurements taken while the CTD pump was not activated, further reducing the number of valid near-surface observations available to CORA relative to ISAS20.

Table 4 and 6 give the RMS differences between CORA and the reference products. The SST RMS difference decreases with time for ERSST and IAPv4, and slightly increases then decreases for EN4. It is worth noting that ERSST, IAPv4 and EN4 SST RMS differences are almost identical during the Argo era, while ISAS20 is smaller by a factor of 1.8. This suggests that the objective-analysis method shared by ISAS20 and CORA tends to produce more consistent interannual variability between the two than either does with the statistically-based products. The SSS RMS difference (for IAPv4 and EN4, the only products with data across all three periods) is low during both the early period and the Argo era, and peaks during 1985-2005 — the same

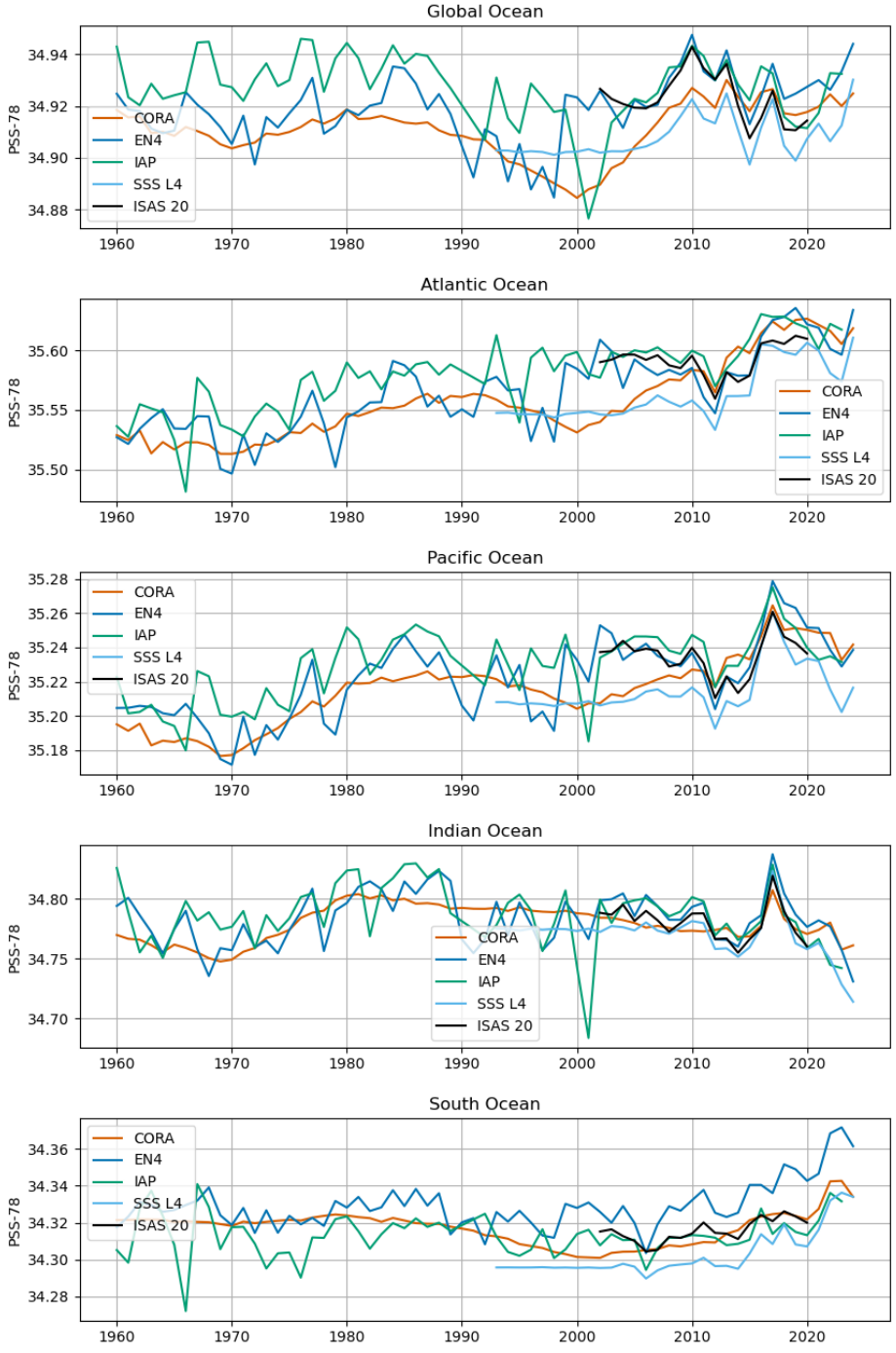


Figure 6. Mean SSS in deep ocean zones for CORA, EN4, IAPv4, SSS L4, and ISAS 20 for the global ocean, Atlantic Ocean, Pacific Ocean , Indian Ocean, and Southern ocean (Latitude <-35°N).

		1960–1984	1985–2005	2006–2020
CORA	Global	0.0017	0.0029	0.0035
	Pacific	0.0029	0.0018	0.0065
	Atlantic	0.0038	0.0035	0.0074
	Indian	0.0031	0.0010	0.0089
	South	0.0007	0.0009	0.0017
EN4	Global	0.0060	0.0086	0.0073
	Pacific	0.010	0.013	0.012
	Atlantic	0.015	0.016	0.011
	Indian	0.0154	0.016	0.017
	South	0.0048	0.0062	0.0061
ERSST	Global	–	–	–
	Pacific	–	–	–
	Atlantic	–	–	–
	Indian	–	–	–
	South	–	–	–
IAP v4	Global	0.0075	0.010	0.0053
	Pacific	0.016	0.013	0.010
	Atlantic	0.019	0.015	0.0094
	Indian	0.017	0.027	0.016
	South	0.013	0.0048	0.0051
ISAS 20	Global	–	–	0.0062
	Pacific	–	–	0.0095
	Atlantic	–	–	0.0086
	Indian	–	–	0.015
	South	–	–	0.0030
SMOS	Global	–	–	0.0067
	Pacific	–	–	0.013
	Atlantic	–	–	0.011
	Indian	–	–	0.017
	South	–	–	0.0043

Table 5. Detrended standard deviation of the SSS by ocean basin and by sub-period

	1960–1984	1985–2005	2006–2020
ERSST	–	–	–
IAPv4	0.0081	0.011	0.0071
EN4	0.0063	0.015	0.0061
ISAS 20	–	–	0.0086
SMOS	–	–	0.0050

Table 6. SSS RMS differences

hump-shaped pattern observed for the OHC RMS differences against GCOS and Cheng et al. (2023), suggesting a common cause (e.g. a transition in the underlying observing network) rather than a variable-specific artifact.

4.3 OHC estimation

In addition to being a key indicator for understanding the evolution of the Earth's climate (Meyssignac et al., 2019; Pan et al., 2025), the intercomparison of various OA products also provides a mean to assess the robustness of individual products and the consistency of their temperature fields (see Liang et al. (2021), for instance). The CORA OHC estimate is compared with the most recent version of the US National Center for Environmental Information (NCEI) (Levitus et al., 2012), an estimate based on IAPv4 (Cheng et al., 2024b), and the estimate produced by the Global Climate Observing System (GCOS) initiative (von Schuckmann et al., 2023).

All the ocean heat content time series, see figure 7, are in very good agreement after 2005, corresponding to the full deployment of the ARGO network (see Fig. 2). During the 1985–2005 period, the spread among the time series is larger, but the warming trends remain consistent. The largest discrepancies occur during the 1960–1984 period. IAPv4, GCOS, and US NCEI estimates vary between –150 and –50 zeta joules, while CORA estimates range from –100 to –50 zeta joules. Nevertheless, the error bars still largely overlap. The comparison of GOHC trends (Table 7) shows a lower trend value for CORA during the 1960-1984 period relative to the other three products, although the spread among all four products in this early period (1.1 ZJ yr^{-1}) is comparable to that of the 2005-2024 period (0.9 ZJ yr^{-1}), rather than markedly larger. The most notable feature of Table 7 is instead the comparatively small interannual variability of the basin-averaged CORA product, further quantified in Table 8 and Table 9. This observation is consistent with Lyman and Johnson (2008) and Cheng and Zhu (2014a), which indicate that OHC time series and their uncertainties are sensitive to changes in OA first guesses and data distribution.

However, when compared to basin-scale OHC estimates from NCEI (not shown), the 1960-1984 positive shift is apparent in the Atlantic Ocean but almost undetectable in the Pacific and Indian Oceans. Data coverage in the Atlantic Ocean was much higher than in the Indian and Pacific Oceans during this period, suggesting that this feature may represent a potential bias in the data. As most of the profiles deployed during this period were bottle casts, we cannot neglect the potential impact of the linear vertical interpolation scheme. Such features have been documented by Li et al. (2022), who noted that linear interpolation of profiles tends to overestimate GOHC calculations by approximately 40 zeta joules before 1990.

	1960-1984	1985-2004	2005-2024
CORA OA	0.7 ± 0.2	5.5 ± 0.1	9.6 ± 0.1
NCEI	1.5 ± 0.1	5.5 ± 0.1	8.7 ± 0.04
GCOS	1.3 ± 0.1	5.9 ± 0.1	8.7 ± 0.07
IAPv4	1.8 ± 0.1	5.5 ± 0.1	9.3 ± 0.04

Table 7. Mean yearly trend of global ocean heat content anomalies (zeta Joules/year)

Table 8 shows that all reference products except CORA OA display a decreasing interannual variability, from about 9 ZJ in the early period to 2.5–5.5 ZJ during the Argo era. CORA OA, by contrast, has the lowest variability of the four products during 1960–1984, peaks during 1985–2005, and plateaus during the Argo era at a level close to GCOS, moderately above IAPv4, and more than twice that of NCEI. This pattern is consistent with the objective-analysis correlation-scale constraint

	1960-1984	1985-2004	2005-2024
NCEI	8.93	5.87	2.54
GCOS	9.04	8.62	5.54
CORA OA	4.18	6.14	5.63
IAPv4	9.28	6.90	4.38

Table 8. Global ocean heat content standard deviation

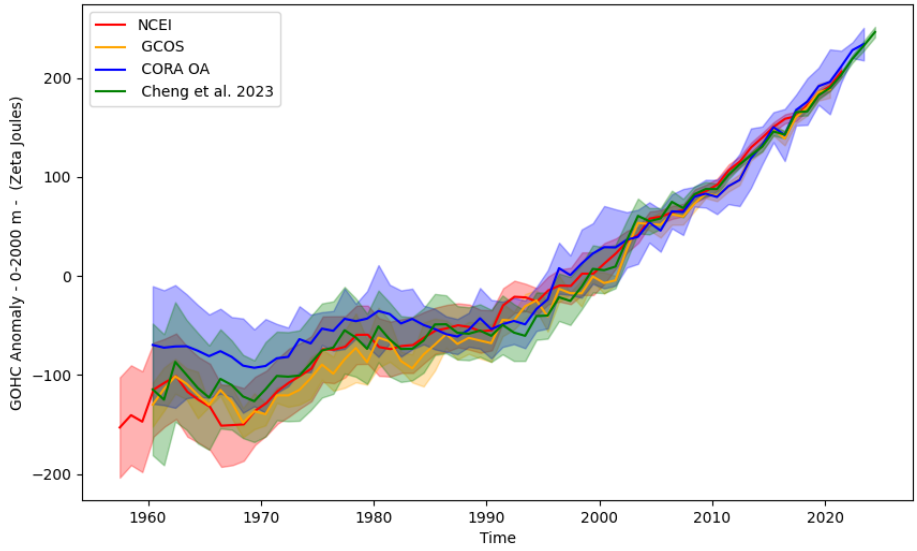


Figure 7. Global ocean heat content anomaly for CORA, and NCEI

being weakly satisfied in the sparse-sampling era, damping the analysis increments toward the background climatology and suppressing spurious interannual noise. On the other hand, the other products appear to retain sampling-driven variability that only recedes once Argo provides dense, homogeneous coverage. Once the correlation-scale constraint is well satisfied in the Argo era, CORA interannual variability settles at a level comparable to or above the other products, suggesting it retains more independent interannual signal than the more strongly statistically-smoothed reference products.

	1960–1984	1985–2005	2006–2020
NCEI	15.95	13.13	8.39
GCOS	8.81	15.00	3.10
IAPv4	10.10	13.17	7.22

Table 9. RMS differences with CORA OA by sub-period

Table 9 gives the RMS differences between CORA and each reference product by sub-period, offering insight into how well interannual anomalies from each product track those of CORA. The three products show markedly different behaviours. The CORA-NCEI RMS difference decreases monotonically from 15.95 ZJ (1960-1984) to 8.39 ZJ (2006-2020). GCOS and IAPv4 , by contrast, follow a non-monotonic, hump-shaped pattern: an intermediate RMS in the early period (8.81 and 10.10 ZJ respectively), a peak in 1985-2005 (15.00 and 13.17 ZJ), and a marked drop during the Argo era (3.10 and 7.22 ZJ), the lowest values of the three periods for both products. The elevated RMS differences before 1985 are consistent with the objective-analysis correlation-scale constraint being weakly satisfied during the sparse-sampling era, which damps CORA OA interannual signal relative to the reference products; however, the contrast between NCEI's monotonic decline and GCOS/IAPv4 hump shape suggests that phase alignment of the interannual anomalies, not only their amplitude, also plays a role and differs by product. The persistence of a 3-8 ZJ residual RMS difference during the Argo era, when sampling is no longer limiting, points to genuine structural/methodological differences between the products (climatology reference, mapping method, QC) rather than a data-coverage effect.

4.4 Steric sea level

The analysis of the mean steric sea level anomaly is key indicator for monitoring the "salty drift" of ARGO floats (Liu et al., 2024), first identified by Wong et al. (2020). This drift affects a large fraction of ARGO floats, introducing a small positive salinity bias. Although this bias is difficult to detect and correct, its impact becomes apparent in halosteric anomaly calculations, which integrate even small errors from deep layers to the surface. Later, the ARGO community attempted to adjust or flag the spurious profiles (Wong et al., 2023), but some effect of the salty drift remains in the 2D gridded fields (Tang et al., 2024; Liu et al., 2024).

Figure 8 shows the time series of the yearly mean halosteric height anomaly (HSSLA) calculated following equation 7. The CORA product exhibits long-term variability similar to EN4 and IAPv4, although with lower interannual variability. The ARGO salty drift contributes to a spread among the products, as noted by (Liu et al., 2024). Following the assumptions of Wong et al. (2020), this spread might decrease after 2022, as the number of ARGO profilers with delayed-time mode adjustments increase and the manufacturing issue responsible for the salty drift has been partly resolved. The ISAS 20 products exhibit variability very similar to CORA, although with a sharp decrease in HSSLA in 2018–2020. This is likely because the ISAS 20 product, produced in 2021, included fewer ARGO floats with delayed-time mode adjustments for those 3 years.

$$HSSL = -\int_0^h \beta(S - \bar{S})dz \tag{7}$$

5 Conclusions

The updated version of the CORA OA product (INSITU_GLO_TS_REP_OBSERVATIONS_013_001 in the Copernicus Marine Service catalogue) now spans the period 1960–2023 and the depth range 0–5500 dbar. It is based on all available in-situ

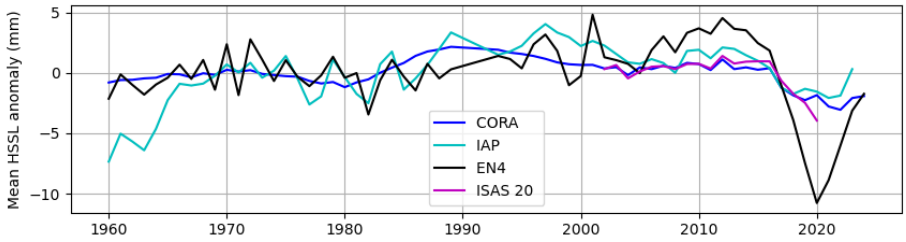


Figure 8. Mean halosteric height anomaly (-60°N, 60°N, 0 to 2000 m depth) for CORA, ISAS 20, IAPv4 and EN4.

profiles distributed through the INSITU_GLO_PHY_TS_DISCRETE_MY_013_001 product CMEMS (2025). The objective analysis method relies on the ISAS-V6 algorithm Gaillard et al. (2016). This work details the objective mapping approach and associated parameters, with a particular focus on defining an appropriate first-guess field to ensure accurate estimates of global ocean heat content.

The product is validated by comparing it with a selection of international reference fields. Parameters such as SST and SSS are evaluated against both in-situ–based gridded products and satellite-derived products. Integrated quantities, including halosteric sea-level anomaly and global ocean heat content, are also assessed to ensure that, once vertically interpolated, the gridded product remains accurate.

The SST validation shows that the objective analysis is in very good overall agreement with the reference products. Global trends are consistent with these references, both at the global scale and at individual basin scales. However, the objective-analysis parameters tend to smooth interannual variability, meaning that this time scale is not well represented in the product—particularly before the Argo era and in sparsely sampled regions. The definition of the correlation function necessarily involves a compromise among large-scale, mesoscale, and unresolved processes. As a result, the effective correlation scale depends on the local and temporal density of ocean observations and should therefore vary substantially in space and time.

The SSS comparison also shows good agreement between CORA OA and the reference products at both global and basin scales, although differences in grid resolution and in the representation of river plumes lead to a large spread among products. This spread decreases markedly with the development of the Argo program and the sharp increase in data availability after 2005.

In contrast, the products based on a near real time processing of ARGO profiles, such as EN4, often lack the effects of the ARGO post processing and exhibit stronger effects of fast salty drift.

Comparisons of global ocean heat content with reference products show an excellent overall fit for the 1985–2024 period. The product however appears to overestimate heat content during the 1960–1984 period, with a bias that decreases from 40 ZJ in 1960 to negligible levels by 1985. The strong correlation between the CORA GOHC anomaly trend and reference products validates the dataset's ability to accurately reflect the impacts of global climate change on marine thermal structures. The effects of the evolution of the ARGO data mode on such metric remain unclear, however the pressure correction of ARGO

floats have shown to have a significant impact on thermosteric level anomaly calculation (Barker et al., 2011), and hence might have an impact of global ocean heat content estimation.

This study demonstrates that although major improvements have been integrated into this new version, further refinements are possible. The most critical priority is the enhancement of the vertical interpolation scheme to reduce the ocean heat content overestimation resulting from the sparse vertical profiles (primarily bottle data) available during this period (Cheng and Zhu (2014b); Li et al. (2022); Barker and McDougall (2020)). A second key improvement would be the update of the XBT correction scheme. It must be highlighted, however, that these two points focus on correcting small but systemic bias-inducing errors in large-scale vertically integrated quantities, such as global ocean heat content. At the individual profile scale, these error sources remain low relative to the product's precision; consequently, local temperature and salinity estimations remain accurate in well-sampled regions for these periods.

6 Data availability

This product is based on the CORA 5.2 dataset (Szekely et al. (2019)), available at https://doi.org/10.17882/46219. The dataset described in this paper is freely available at https://doi.org/10.48670/mds-00383.

7 Code availability

The Python and Fortran 90 codes used to perform this analysis are openly available under the MIT licence at https://doi.org/10.5281/zenodo.20824880.

Acknowledgements. This study has been conducted using E.U. Copernicus Marine Service. The authors wish to thank the members of the Copernicus Marine Service In Situ Thematic Assembly Centre (In Situ TAC) for their valuable feedback and constructive discussions. The In Situ TAC is coordinated by Ifremer (France) and brings together the expertise of 16 European institutes, including Puertos del Estado, HCMR, IOBAS, IMR, SMHI, BSH, Coriolis, SOCIB, CLS, SYKE, MetOffice, OGS, the University of Bergen, and Azti. Their collective effort in providing consistent, quality-controlled ocean in situ observations greatly supported the present work. The authors would also like to extend their sincere gratitude to Dominique Aubaton for his careful reviews and insightful advice, which greatly contributed to the writing of this manuscript.

The authors declare that AI-assisted tools (Claude, Anthropic and Chat GPT-4, OpenAI) were used during the preparation of this manuscript to improve the grammar, clarity, and accuracy of the text. The scientific content, data analysis, and conclusions remain entirely the responsibility of the authors.

References

Pierre Bahurel, Fabio Adragna, M. J. Bell, Fabrice Jacq, Johnny A. Johannessen, Pierre-Yves Le Traon, Jun She, et al. Ocean monitoring and forecasting core services: The european myocean example. In *Proceedings of OceanObs'09: Sustained Ocean Observations and Information for Society*, volume 2, pages 21–25, Venice, Italy, 2010. ESA Publication WPP-306. doi available in proceedings.

Paul Barker, Jeff Dunn, Catia Domingues, and Susan Wijffels. Pressure sensor drifts in argo and their impacts. *Journal of Atmospheric and Oceanic Technology - J ATMOS OCEAN TECHNOL*, 28:1036–1049, 08 2011. https://doi.org/10.1175/2011JTECHO831.1.

Paul M. Barker and Trevor J. McDougall. Two interpolation methods using multiply-rotated piecewise cubic hermite interpolating polynomials. *Journal of Atmospheric and Oceanic Technology*, 37(4):605–619, 2020. https://doi.org/10.1175/jtech-d-19-0211.1. URL https://doi.org/10.1175/jtech-d-19-0211.1.

Bernard Bourlès, Rick Lumpkin, Michael J. McPhaden, Fabrice Hernandez, Paulo Nobre, and et al. The pirata program: History, accomplishments, and future directions. *Bulletin of the American Meteorological Society*, 89(8):1111–+, 2008. https://doi.org/10.1175/2008BAMS2462.1.

J. Boutin, N. Reul, J. Koehler, A. Martin, R. Catany, S. Guimbard, et al. Satellite-based sea surface salinity designed for ocean and climate studies. *Journal of Geophysical Research: Oceans*, 126:e2021JC017676, 2021. https://doi.org/10.1029/2021JC017676. URL https://doi.org/10.1029/2021JC017676.

F.P. Bretherton, R.E. Davis, and C.B. Fandry. A technique for objective analysis and design of oceanographic experiments applied to mode-73. *Deep Sea Research and Oceanographic Abstracts*, 23(7):559–582, 1976. https://doi.org/10.1016/0011-7471(76)90001-2.

C. Cabanes, A. Grouazel, K. von Schuckmann, M. Hamon, V. Turpin, C. Coatanoan, F. Paris, S. Guinehut, C. Boone, N. Ferry, C. de Boyer Montégut, T. Carval, G. Reverdin, S. Pouliquen, and P.-Y. Le Traon. The cora dataset: validation and diagnostics of in-situ ocean temperature and salinity measurements. *Ocean Science*, 9:1–18, 2013. https://doi.org/10.5194/os-9-1-2013.

Piers Chapman. The world ocean circulation experiment (woce). *Marine Technology Society Journal*, 32(3):23, 1998. Fall 1998; ProQuest.

L. Cheng and J. Zhu. Artifact in variations of ocean heat content induced by the observation system changes. *Geophys. Res. Lett.*, 41: 7276–7283, 2014a. https://doi.org/10.1002/2014GL061881.

L. Cheng, J. Zhu, R. Cowley, T. Boyer, and S. Wijffels. Time, probe type, and temperature variable bias corrections to historical expendable bathythermograph observations. *Journal of Atmospheric and Oceanic Technology*, 31:1793–1825, 2014. https://doi.org/10.1175/JTECH-D-13-00197.1.

L. Cheng, G. Foster, Z. Hausfather, K. E. Trenberth, and J. Abraham. Improved quantification of the rate of ocean warming. *J. Climate*, 35: 4827–4840, 2022a. https://doi.org/10.1175/JCLI-D-21-0895.1.

L. Cheng, K. von Schuckmann, J. P. Abraham, et al. Past and future ocean warming. *Nature Reviews Earth & Environment*, 3:776–794, 2022b. https://doi.org/10.1038/s43017-022-00345-1.

L. Cheng, Y. Pan, Z. Tan, H. Zheng, Y. Zhu, W. Wei, J. Du, H. Yuan, G. Li, H. Ye, V. Gouretski, Y. Li, K. E. Trenberth, J. Abraham, Y. Jin, F. Reseghetti, X. Lin, B. Zhang, G. Chen, M. E. Mann, and J. Zhu. Iapv4 ocean temperature and ocean heat content gridded dataset. *Earth Syst. Sci. Data*, 16:3517–3546, 2024a. https://doi.org/10.5194/essd-16-3517-2024.

L. Cheng, K. von Schuckmann, A. Minière, et al. Ocean heat content in 2023. *Nature Reviews Earth & Environment*, 5:232–234, 2024b. https://doi.org/10.1038/s43017-024-00539-9. URL https://doi.org/10.1038/s43017-024-00539-9.

Lijing Cheng and Jiang Zhu. Uncertainties of the ocean heat content estimation induced by insufficient vertical resolution of historical ocean subsurface observations. *Journal of Atmospheric and Oceanic Technology*, 31(6):1383–1396, 2014b. https://doi.org/10.1175/JTECH-D-13-00220.1. URL https://doi.org/10.1175/JTECH-D-13-00220.1.

CMEMS. Insitu_glo_phy_ts_discrete_my_013_001. https://doi.org/10.17882/46219, 2025. (accessed on 01-12-2025).

S. Fournier, J. Vialard, M. Lengaigne, T. Lee, M. M. Gierach, and A. V. S. Chaitanya. Modulation of the ganges-brahmaputra river plume by the indian ocean dipole and eddies inferred from satellite observations. *Journal of Geophysical Research: Oceans*, 122(12): 9591–9604, 2017. https://doi.org/https://doi.org/10.1002/2017JC013333. URL https://agupubs.onlinelibrary.wiley.com/doi/abs/10.1002/2017JC013333.

F. Gaillard. Isas-tool version 6: Method and configuration. Technical Report LPO-12-02, Ifremer, 2012.

F. Gaillard, E. Autret, V. Thierry, P. Galaup, C. Coatanoan, and T. Loubrieu. Quality control of large argo datasets. *Journal of Atmospheric and Oceanic Technology*, 26:337–351, 2009. https://doi.org/10.1175/2008JTECHO552.1.

F. Gaillard, T. Reynaud, V. Thierry, N. Kolodziejczyk, and K. von Schuckmann. In situ–based reanalysis of the global ocean temperature and salinity with isas: Variability of the heat content and steric height. *Journal of Climate*, 29:1305–1323, 2016. https://doi.org/10.1175/JCLI-D-15-0028.1.

S. A. Good, M. J. Martin, and N. A. Rayner. En4: quality controlled ocean temperature and salinity profiles and monthly objective analyses with uncertainty estimates. *Journal of Geophysical Research: Oceans*, 118:6704–6716, 2013. https://doi.org/10.1002/2013JC009067.

J. Gourrion, T. Szekely, R. Killick, B. Owens, G. Reverdin, and B. Chapron. Improved statistical method for quality control of hydrographic observations. *Journal of Atmospheric and Oceanic Technology*, 37, 2020. https://doi.org/10.1175/JTECH-D-18-0244.1.

B. Huang, X. Yin, J. A. Carton, L. Chen, G. Graham, P. Hogan, et al. Record high sea surface temperatures in 2023. *Geophysical Research Letters*, 51:e2024GL108369, 2024. https://doi.org/10.1029/2024GL108369.

B. Huang, Chunying Liu Matthew Menne Yuhan Douglas Rao Thomas Smith Russell Vose Xungang Yin, Tim Boyer, and Huai-Min Zhang. Extended reconstructed sea surface temperature, version 6 (ersstv6). part i: An artificial neural network approach. *J. Climate*, 38:1105–1121, 2025. https://doi.org/10.1175/JCLI-D-23-0707.1.

IPCC. Climate Change 2023: Synthesis Report. Contribution of Working Groups I, II and III to the Sixth Assessment Report of the Intergovernmental Panel on Climate Change, 2023.

Steven R. Jayne, Dean Roemmich, Nathalie Zilberman, Stephen C. Riser, Kenneth S. Johnson, Gregory C. Johnson, and Stephen R. Piotrowicz. The argo program present and future. *Oceanography*, 30(2):18–28, 2017. Special Issue on Autonomous and Lagrangian Platforms and Sensors: Current and Future Directions in Ocean Sampling (June 2017).

Rachel Killick. *EN.4.2.2 Product User Guide*, August 2021. First EN4 Product User Guide, Version number incremented when changes are made to the documentation for additions or EN4 version updates.

N. Kolodziejczyk, A. Prigent-Mazella, and F. Gaillard. Isas temperature, salinity, dissolved oxygen gridded fields, 2019.

Nicolas Kolodziejczyk, Annaig Prigent-Mazella, and Fabienne Gaillard. Isas temperature, salinity, dissolved oxygen gridded fields, 2023. URL https://doi.org/10.17882/52367.

P.-Y. Le Traon, A. Reppucci, E. Alvarez Fanjul, L. Aouf, A. Behrens, M. Belmonte, A. Bentamy, L. Bertino, V. E. Brando, M. B. Kreiner, M. Benkiran, T. Carval, S. A. Ciliberti, H. Claustre, E. Clementi, G. Coppini, G. Cossarini, M. De Alfonso Alonso-Muñoyerro, A. Delamarche, G. Dibarboure, F. Dinessen, M. Drevillon, Y. Drillet, Y. Faugere, V. Fernández, A. Fleming, M. I. Garcia-Hermosa, M. G. Sotillo, G. Garric, F. Gasparin, C. Giordan, M. Gehlen, M. L. Gregoire, S. Guinehut, M. Hamon, C. Harris, F. Hernandez, J. B. Hinkler, J. Hoyer, J. Karvonen, S. Kay, R. King, T. Lavergne, B. Lemieux-Dudon, L. Lima, C. Mao, M. J. Martin, S. Masina, A. Melet, B. Buon-

giorno Nardelli, G. Nolan, A. Pascual, J. Pistoia, A. Palazov, J.-F. Piolle, M. I. Pujol, A.-C. Pequignet, E. Peneva, B. Pérez Gómez, L. Petit de la Villeon, N. Pinardi, A. Pisano, S. Pouliquen, R. Reid, E. Remy, R. Santoleri, J. Siddorn, J. She, J. Staneva, A. Stoffelen, M. Tonani, L. Vandenbulcke, K. von Schuckmann, G. Volpe, C. Wettre, and A. Zacharioudaki. From observation to information and users: The copernicus marine service perspective. *Frontiers in Marine Science*, 6:234, 2019. https://doi.org/10.3389/fmars.2019.00234.

Jean-Michel Lellouche, Eric Greiner, Romain Le Brehon-Bretonniere, Gilles Garric, Angélique Melet, Marie Drillet, Clément Bourdallé-Badie, Mathieu Hamon, Olivier Le Galloudec, Charly Regnier, Tony Candela, Charles-Emmanuel Talandier, Florent Testut, Giovanni Ruggiero, Mounir Benkiran, Yann Drévillon, and Pierre-Yves Le Traon. The copernicus global 1/12° oceanic and sea ice glorys12 reanalysis. *Frontiers in Earth Science*, 9:698876, 2021. https://doi.org/10.3389/feart.2021.698876.

S. Levitus, J. I. Antonov, T. P. Boyer, O. K. Baranova, H. E. Garcia, R. A. Locarnini, A. V. Mishonov, J. R. Reagan, D. Seidov, E. S. Yarosh, and M. M. Zweng. World ocean heat content and thermosteric sea level change (0–2000 m) 1955–2010. *Geophysical Research Letters*, 39:L10603, 2012. https://doi.org/10.1029/2012GL051106.

Yuehua Li, John A. Church, Trevor J. McDougall, and Paul M. Barker. Sensitivity of observationally based estimates of ocean heat content and thermal expansion to vertical interpolation schemes. *Geophysical Research Letters*, 49(24):e2022GL101079C, 2022. https://doi.org/10.1029/2022GL101079C. URL https://doi.org/10.1029/2022GL101079C. Open Access, Research Letter.

Xinfeng Liang, Chao Liu, Rui M. Ponte, and Don P. Chambers. A comparison of the variability and changes in global ocean heat content from multiple objective analysis products during the argo period. *J. Climate*, 34:7875–7895, 2021. https://doi.org/10.1175/JCLI-D-20-0794.1.

Chao Liu, Xinfeng Liang, Rui M. Ponte, and Don P. Chambers. "salty drift" of argo floats affects the gridded ocean salinity products. *Journal of Geophysical Research: Oceans*, 129(9), 2024. https://doi.org/10.1029/2023JC020871. License CC BY-NC 4.0.

J. M. Lyman and G. C. Johnson. Estimating annual global upper-ocean heat content anomalies despite irregular in situ ocean sampling. *J. Clim.*, 21:5629–5641, 2008. https://doi.org/10.1175/2008JCLI2259.1.

B. Meyssignac, T. Boyer, Z. Zhao, M. Z. Hakuba, F. W. Landerer, D. Stammer, A. Köhl, S. Kato, T. L'Ecuyer, M. Ablain, J. P. Abraham, A. Blazquez, A. Cazenave, J. A. Church, R. Cowley, L. Cheng, C. M. Domingues, D. Giglio, V. Gouretski, M. Ishii, G. C. Johnson, R. E. Killick, D. Legler, W. Llovel, J. Lyman, M. D. Palmer, S. Piotrowicz, S. G. Purkey, D. Roemmich, R. Roca, A. Savita, K. von Schuckmann, S. Speich, G. Stephens, G. Wang, S. E. Wijffels, and N. Zilberman. Measuring global ocean heat content to estimate the earth energy imbalance. *Frontiers in Marine Science*, 6:432, 2019. https://doi.org/10.3389/fmars.2019.00432.

P. P. Niiler. The world ocean surface circulation. In G. Siedler, J. Church, and J. Gould, editors, *Ocean Circulation and Climate*, volume 77 of *International Geophysics Series*, pages 193–204. Academic Press, 2001.

Y. Pan, A. Minière, K. von Schuckmann, et al. Ocean heat content in 2024. *Nature Reviews Earth & Environment*, 6:249–251, 2025. https://doi.org/10.1038/s43017-025-00655-0. URL https://doi.org/10.1038/s43017-025-00655-0.

James R. Reagan, Tim P. Boyer, Hernán E. García, Ricardo A. Locarnini, Olga K. Baranova, Courtney Bouchard, Scott L. Cross, Alexey V. Mishonov, Christopher R. Paver, Dan Seidov, Zhankun Wang, and Dmitry Dukhovskoy. World ocean atlas 2023, 2024. NOAA National Centers for Environmental Information.

Dean Roemmich, Gregory C. Johnson, Stephen Riser, Russ Davis, John Gilson, W. Brechner Owens, Silvia L. Garzoli, Claudia Schmid, and Mark Ignaszewski. The argo program: Observing the global ocean with profiling floats. *Oceanography*, 22(2):34–43, 2009. Special Issue on the Tenth Anniversary of the National Oceanographic Partnership Program (June 2009).

Michela Sammartino, Salvatore Aronica, Rosalia Santoleri, and Bruno Buongiorno Nardelli. Retrieving mediterranean sea surface salinity distribution and interannual trends from multi-sensor satellite and in situ data. *Remote Sensing*, 14(2502), 2022.

Wei Shi and Menghua Wang. Monitoring the amazon river plume from satellite observations. *GIScience & Remote Sensing*, 61(1):2416725, 2024. https://doi.org/10.1080/15481603.2024.2416725. URL https://doi.org/10.1080/15481603.2024.2416725.

T. Szekely. *In Situ TAC Objective Analysis Product*, 2024a. Contributors: T. Szekely.

T. Szekely. Delayed time mode validation: Minimum / maximum temperature and salinity reference field, 2024b.

T. Szekely, J. Gourrion, S. Pouliquen, and G. Reverdin. The cora 5.2 dataset for global in situ temperature and salinity measurements: data description and validation. *Ocean Science*, 15(6):1601–1614, 2019. https://doi.org/10.5194/os-15-1601-2019. URL https://os.copernicus.org/articles/15/1601/2019/.

L. Tang, H. Zhou, J. Li, P. Wang, X. Su, and Z. Luo. Effect of argo salinity drift since 2016 on the estimation of regional steric sea level change rates. *Remote Sensing*, 16(11):1855, 2024. https://doi.org/10.3390/rs16111855.

C.-C. Teng, L. Bernard, L. LeBlanc, B. Hansen, and R. Crout. Test and evaluation of refreshed tropical atmosphere ocean (tao) buoy system. In *OCEANS 2008 - MTS/IEEE Kobe Techno-Ocean*, pages 1–7, Kobe, Japan, 2008. https://doi.org/10.1109/OCEANSKOBE.2008.4531027.

J. Terhaar, F. A. Burger, L. Vogt, et al. Record sea surface temperature jump in 2023–2024 unlikely but not unexpected. *Nature*, 639:942–946, 2025. https://doi.org/10.1038/s41586-025-08674-z.

H.L. Varona, D. Veleda, M. Silva, M. Cintra, and M. Araujo. Amazon river plume influence on western tropical atlantic dynamic variability. *Dynamics of Atmospheres and Oceans*, 85:1–15, 2019. ISSN 0377-0265. https://doi.org/https://doi.org/10.1016/j.dynatmoce.2018.10.002. URL https://www.sciencedirect.com/science/article/pii/S0377026517300866.

K. von Schuckmann and P.-Y. Le Traon. How well can we derive global ocean indicators from argo data? *Ocean Science*, 7:783–791, 2011. https://doi.org/10.5194/os-7-783-2011.

K. von Schuckmann, A. Minière, F. Gues, F. J. Cuesta-Valero, G. Kirchengast, S. Adusumilli, F. Straneo, M. Ablain, R. P. Allan, P. M. Barker, H. Beltrami, A. Blazquez, T. Boyer, L. Cheng, J. Church, D. Desbruyeres, H. Dolman, C. M. Domingues, A. García-García, D. Giglio, J. E. Gilson, M. Gorfer, L. Haimberger, M. Z. Hakuba, S. Hendricks, S. Hosoda, G. C. Johnson, R. Killick, B. King, N. Kolodziejczyk, A. Korosov, G. Krinner, M. Kuusela, F. W. Landerer, M. Langer, T. Lavergne, I. Lawrence, Y. Li, J. Lyman, F. Marti, B. Marzeion, M. Mayer, A. H. MacDougall, T. McDougall, D. P. Monselesan, J. Nitzbon, I. Otosaka, J. Peng, S. Purkey, D. Roemmich, K. Sato, K. Sato, A. Savita, A. Schweiger, A. Shepherd, S. I. Seneviratne, L. Simons, D. A. Slater, T. Slater, A. K. Steiner, T. Suga, T. Szekely, W. Thiery, M.-L. Timmermans, I. Vanderkelen, S. E. Wjiffels, T. Wu, and M. Zemp. Heat stored in the earth system 1960–2020: where does the energy go? *Earth System Science Data*, 15(4):1675–1709, 2023. https://doi.org/10.5194/essd-15-1675-2023. URL https://essd.copernicus.org/articles/15/1675/2023/.

Karina von Schuckmann, Jean-Baptiste Sallée, D. Chambers, Pierre-Yves Le Traon, C. Cabanes, et al. Monitoring ocean heat content from the current generation of global ocean observing systems. *Ocean Science Discussions*, 10:923–949, 2013. https://doi.org/10.5194/osd-10-923-2013.

A. P. Wong, S. E. Wijffels, S. C. Riser, S. Pouliquen, S. Hosoda, D. Roemmich, and et al. Argo data 1999–2019: Two million temperature–salinity profiles and subsurface velocity observations from a global array of profiling floats. *Frontiers in Marine Science*, 7:700, 2020. https://doi.org/10.3389/fmars.2020.00700.

Annie P. S. Wong, John Gilson, and Cécile Cabanes. Argo salinity: bias and uncertainty evaluation. *Earth Syst. Sci. Data*, 15:383–393, 2023. https://doi.org/10.5194/essd-15-383-2023.